Inorganic Chemistry

Article

pubs.acs.org/IC

Cyclometalated Fe(II) Complexes as Sensitizers in Dye-Sensitized Solar Cells

Sriparna Mukherjee, David N. Bowman, and Elena Jakubikova*

Department of Chemistry, North Carolina State University, Raleigh, North Carolina 27695, United States

Supporting Information

ABSTRACT: Dye-sensitized solar cells (DSSCs) often utilize transition metal-based chromophores for light absorption and semiconductor sensitization. Ru(II)-based dyes are among the most commonly used sensitizers in DSSCs. As ruthenium is both expensive and rare, complexes based on cheaper and more abundant iron could serve as a good alternative. In this study, we investigate Fe(II)-bis(terpyridine) and its cyclometalated analogues, in which pyridine ligands are systematically replaced by aryl groups, as potential photosensitizers in DSSCs. We employ density functional theory at the B3LYP/6-31G*,SDD level to obtain the ground state electronic structure of these complexes. Quantum dynamics simulations are utilized to study interfacial electron transfer between the Fe(II) photosensitizers and a titanium dioxide semiconductor. We find that cyclometalation stabilizes the singlet ground state of these complexes by 8−19 kcal/mol but reduces the electron density on the carboxylic acid attached to the aryl ring. The results suggest that cyclometalation provides a feasible route to increasing the efficiency of Fe(II) photosensitizers but that care should be taken in choosing the substitution position for the semiconductor anchoring group.

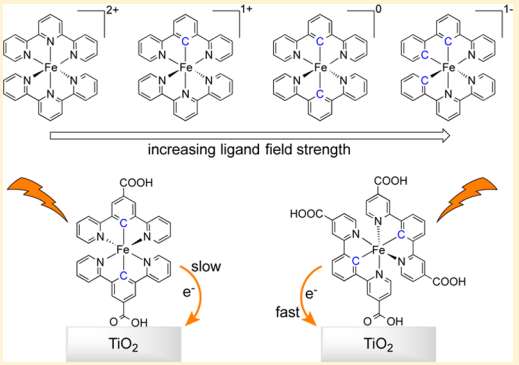

1. INTRODUCTION

Dye-sensitized solar cells (DSSCs) are a cheaper alternative to conventional crystalline semiconductor-based solar cells thanks to their low fabrication cost.[1−5] In contrast to conventional solar cells, the component (dye) responsible for the light absorption process in DSSCs is separated from the components involved in the transportation of charge carriers (electrons and holes).[2,3] Grätzel and co-workers have utilized numerous Ru(II)-polypyridines as sensitizers in DSSCs, reaching device efficiencies of over 10%.[4−8] Replacing Ru(II) in the polypyridyl dye with environmentally benign and earth-abundant Fe(II) can further reduce the cost of DSSCs.

The ability of Fe(II)-polypyridines to photosensitize TiO_2 was first demonstrated by Ferrere and Gregg in a system in which $[Fe(bpy\text{-}dca)_2CN_2]$ (bpy-dca = 2,2′-bipyridine-4,4′-dicarboxylic acid) dye is attached to TiO_2 via the carboxylic acid linker.[9] This system exhibits band-selective sensitization from the initially excited short-lived metal-to-ligand charge transfer (MLCT) states, indicating that sensitization is possible even for complexes that do not possess long-lived photoactive excited states. Subsequently, the effect of solvent and different substituents on the absorption properties of $[Fe(L)_2CN_2]$ (L = substituted 2,2′-bipyridine) was studied, showing that a carboxylic acid linker couples the dye to TiO_2 more efficiently than a phosphonic acid linker.[10] Later, Meyer and co-workers reported two possible sensitization mechanisms in $[Fe(bpy)(CN)_4]^{2-}$-TiO_2 assemblies: (1) direct sensitization in which an electron is excited from the Fe(II) center directly into Ti(IV) sites on TiO_2 and (2) indirect sensitization involving interfacial electron transfer (IET) from the initially populated MLCT states of the dye into the conduction band (CB) of TiO_2.[11] Direct semiconductor sensitization was also observed by Lian and co-workers employing non-polypyridyl Fe(II) dyes such as $[Fe(CN)_6]^{4-}$.[12]

Despite the initially promising results, Fe(II)-polypyridine chromophores are not popular because Fe(II)-sensitized solar cells have a very low overall efficiency compared to that of their Ru(II)-based analogues. The main problem with the utilization of Fe(II) dyes in DSSCs is their low ligand field strength that results in the presence of a low-lying metal-centered (MC) ^5T state in these complexes. Upon initial photoexcitation from the ^1A ground state into a manifold of photoactive MLCT states, Fe(II)-polypyridine dyes undergo intersystem crossing (ISC) into the metal-centered ^5T state on a subpicosecond time scale.[13−16] The MC states are photoinactive and unable to undergo IET into the semiconductor.[17,18] The short lifetime of the photoactive ^{1,3}MLCT states thus represents the main obstacle to the utilization of Fe(II)-polypyridines as a sensitizer in DSSCs.[9,10,14−16]

There are at least two possible routes toward improving the efficiency of Fe(II)-sensitized solar cells. The first route endeavors to increase the rate of IET so that it becomes more competitive with the ISC process. We have recently shown that the IET rate in Fe(II) dye-semiconductor

Received: October 4, 2014
Published: December 22, 2014

DOI: 10.1021/ic502438g
Inorg. Chem. 2015, 54, 560−569

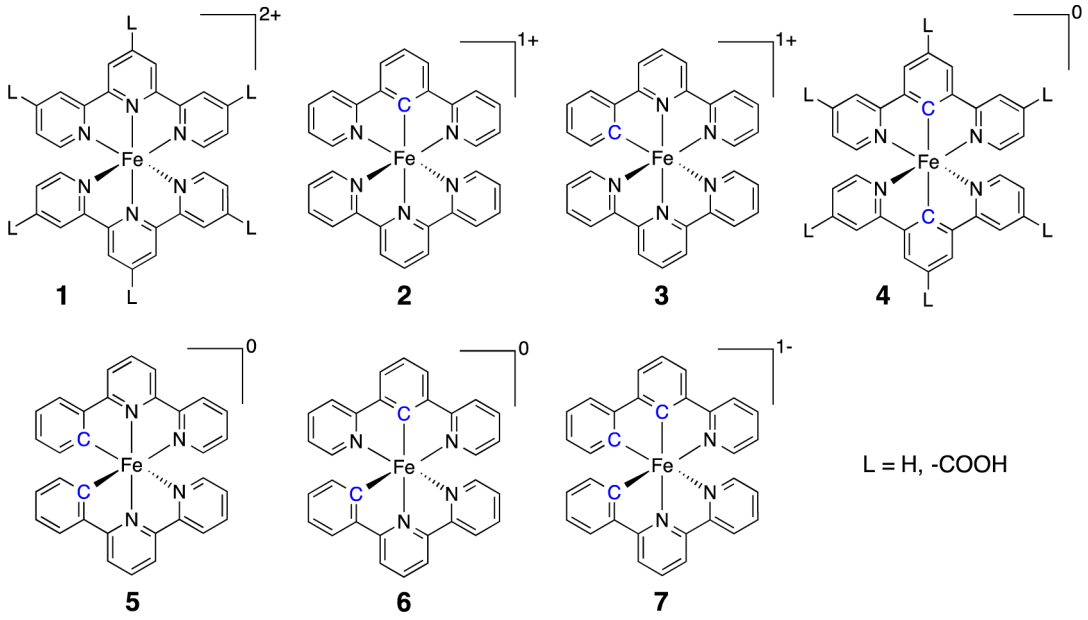

Figure 1. $[Fe(tpy)_2]^{2+}$ (complex **1**) and its cyclometalated analogues **2**−**7** investigated in this study.

assemblies can be tuned by a judicious choice of the semiconductor anchoring group.[19]

The approach undertaken in this work aims to increase the lifetime of photoactive MLCT states by slowing or completely eliminating ISC so that IET becomes a dominant decay pathway. This can be achieved in principle for Fe(II)-polypyridines by synthetic modifications that increase the ligand field strength of the coordinating ligands. Wärnmark, Sundström, Persson, and co-workers have shown the presence of a long-lived excited state (τ_{ISC} = 9 ps) in an Fe(II) complex with N-heterocyclic carbene ligands $[Fe(CNC)_2]^{2+}$ (CNC = 2,6-bis(3-methylimidazole-1-ylidine)pyridine).[20,21] McCusker and co-workers have reported an approach to the $^5T/^3T$ crossing point in the $[Fe(dcpp)_2]^{2+}$ (dcpp = 2,6-bis(2-carboxypyridyl)pyridine) complex that displays an almost ideal octahedral geometry.[22] Computational studies by Dixon et al. also suggest that the presence of one or two Fe−C bonds in cyclometalated Fe(II)-bisterpyridine complexes will have beneficial effects on their light-harvesting properties.[23,24]

This work presents a computational study of a series of cyclometalated Fe(II)-polypyridine complexes. All complexes are derived from the $[Fe(tpy)_2]^{2+}$ parent complex (tpy = 2,2′;6′,2″-terpyridine), in which the neutral pyridine groups are systematically replaced by negatively charged aryl moieties (Figure 1). Complex **7** was chosen as the only representative of triply cyclometalated Fe(II) complexes because we expected to see the largest impact on the ligand field strength when the three Fe−C bonds were placed along three different axes. The aim is to determine the changes in the ligand field strength of these complexes upon cyclometalation characterized by $^1A-^5T$ energy differences, as well as to explore their ability to sensitize the TiO_2 semiconductor.

2. METHODS

2.1. Molecular Structure Optimization and Ground State Spin Multiplicity. Complex **1** and its cyclometalated analogues **2**−**7** (Figure 1) were optimized in their singlet and quintet states employing the B3LYP functional[25−27] with the SDD effective core potential and associated basis set for Fe[28] and the 6-31G* basis set for all other atoms (C, H, O, and N).[29,30] Homoleptic complexes with carboxylic acid at the 4′ position of the terpyridine-based ligand (**1a**, **4a**), the 4 and 4″ positions (**1b**, **4b**), and the 4, 4′, and 4″ positions (**1c**, **4c**) were fully optimized utilizing the same methodology (Figure S8 in the Supporting Information (SI)). Optimizations were carried out in vacuum using an ultrafine grid. Vibrational frequency analysis was performed at every optimized structure to confirm that potential energy minima were found. For the high-spin states, natural population analysis[31] was performed to verify a metal-centered electronic state. All calculations on the molecular complexes were carried out using Gaussian09.[32]

Hybrid density functional theory (DFT) functionals (e.g., B3LYP) often incorrectly favor the high-spin state as the ground state.[33] In general, the calculated relative stabilities of high-spin and low-spin states depend on the amount of Hartree−Fock exact exchange used in the hybrid functional.[33,34] In this study, ground state multiplicity of cyclometalated complexes **2**−**7** was determined by comparison to complex **1** using an approach discussed in a previous work.[33] The energy differences ($\Delta E_{HS/LS}$, HS/LS = high-spin/low-spin) between the optimized singlet and quintet states of complexes **1**−**7**, defined as

$$\Delta E_{HS/LS} = E_{quintet} - E_{singlet} \quad (1)$$

where $E_{quintet}$ is the total energy of the fully optimized ^5T state and $E_{singlet}$ is the total energy of the fully optimized ^1A state, were calculated at differing amounts of exact exchange (0, 5, 10, 15, 20, and 25%) present in the B3LYP functional. The trends in $\Delta E_{HS/LS}$ relative to the admixture of exact exchange (c_1) for complexes **2**−**7** were then compared to that of complex **1**, which is known to be singlet in its ground state.

2.2. Dye-Semiconductor Assemblies. All periodic system optimizations were performed using the Vienna Ab initio Simulation Package (VASP).[35−38] These calculations were performed at the PBE[39,40] level of theory with the projector augmented wave method[41] and basis set expansion terminated at 500 eV. As we previously reported,[17,18] the unit cell for bulk anatase was obtained with 13 × 13 × 13 *k*-point sampling. The tetragonal lattice was found to have lattice vectors of $a = b = 3.81$ Å and $c = 9.77$ Å. The unit cell was extended and cut at the (101) surface and functionalized by pyridine-4-carboxylic acid[17,18] or benzoic acid in either monodentate or bidentate binding modes. The isonicotinic acid-TiO_2 and benzoic acid-TiO_2 assemblies were relaxed along with the top two layers of Ti and the top four layers of O using 5 × 3 × 1 *k*-point sampling with lattice vectors of $a = 15.25$ Å, $b = 10.49$ Å, and $c = 26.00$ Å.

DOI: 10.1021/ic502438g
Inorg. Chem. 2015, 54, 560−569

Complexes **1a**, **4a**, **4b**, **4c**, and **4c′** were optimized with the carboxylic acid group, and the lower half of the pyridine or aryl ring (three carbon and two hydrogen atoms) was constrained at surface-optimized geometries. These nonperiodic constrained optimizations were performed employing the Gaussian09 software package at the B3LYP/SDD 6-31G* level of theory. The dyes were then attached to the extended TiO_2 surface using the pyridine-TiO_2 or aryl-TiO_2 structures as a reference,[42] resulting in a dye-TiO_2 supercell with dimensions of 30.49 × 31.46 × 40.00 Å^3.

2.3. Interfacial Electron Transfer Simulations. Interfacial electron transfer (IET) in dye-semiconductor assemblies (**1a**-, **4a**-, **4b**-, **4c**-, and **4c′**-TiO_2) was investigated by means of quantum dynamics simulations, in which the time-dependent electronic wave function $|\Psi(t)\rangle$ is propagated according to the extended Hückel (EH) Hamiltonian.[17,18,43−46] The methodology is described in detail in refs 45 and 46.

Excited states of Fe(II)-polypyridine complexes in the visible spectral region serve as initial states for IET and are generally assigned to d → π^* transitions into the low-lying polypyridine-localized π^* orbitals.[17,18,47,48] Time-dependent density functional theory (TD-DFT) calculations were employed in our previous studies of Fe(II)-polypyridine-TiO_2 assemblies to determine which virtual orbitals become populated upon visible excitations.[17−19] The appropriate virtual orbitals were then used to construct the initial states for IET simulations. However, TD-DFT is unable to properly reproduce the absorption spectrum of the $[Fe(tpy)_2]^{2+}$ complex.[47] For example, TD-DFT spectra obtained at the B3LYP level of theory do not describe the intense peak found in the lower energy region of the experimental spectra at around 540 nm (ref 49 and Figure S9 in the SI).[49] Therefore, we have chosen not to create the initial states based on the TD-DFT results, which is in contrast to our previous work.[17,18,50] The initial states for the IET simulations, $|\Psi(0)\rangle$, were constructed from EH virtual orbitals that match LUMO through LUMO+7 Kohn−Sham (KS) orbitals obtained from the ground state DFT calculations. LUMO through LUMO+7 KS orbitals correspond to the lowest energy virtual orbitals with π^* character and act as representative states for the low-lying polypyridine-localized π^* orbitals that become populated upon excitation. Although this change in the computational protocol allows us to compare the efficiency of IET processes in various dye-semiconductor assemblies, it prevents us from associating IET rates with the absorption bands in the visible region and from calculating theoretical internal quantum efficiencies in **1**-TiO_2 and **4**-TiO_2 assemblies.[17−19]

Alvarez's parameter set[51] employed in the EH calculations was reparameterized to obtain the best match between the KS and EH orbitals for complexes **4a**−**c′**, with nodal structure and energy ordering of the KS orbitals obtained from the B3LYP/SDD,6-31G* calculations as a reference. The modified parameters employed in EH calculations can be found in Table S1 of the SI. The default, unmodified Alvarez's parameter set was employed for calculations on complex **1a**, as the EH orbitals provided a satisfactory match for the KS orbitals.

The initial states for the IET simulations (i.e., LUMO−LUMO+7 EH orbitals of the dye) evolved over time according to the time-dependent Schrödinger equation for the entire dye-TiO_2 system. Survival probability, or the probability that at time t the electron is still localized on the dye, was determined by projecting the time-evolved electronic wave function of the dye-TiO_2 system onto the atomic orbitals of the dye at each simulation step.[45]

All quantum dynamic simulations were run for 2 ps with a time step of 0.1 fs in vacuum at a frozen geometry. Periodic boundary conditions with the super cell of 30.49 × 31.46 × 40.00 Å^3 dimensions and k-point sampling of 1 × 1 × 1 were utilized in all calculations. Absorbing potentials corresponding to the imaginary terms in the diagonal elements of the Hamiltonian were assigned to the bottom layer of Ti to prevent artificial recurrences in the electron-transient population.

Survival probabilities obtained from the IET simulations were fit to a linear combination of exponential functions according to the expression

$$P(t) = \sum_{i=1}^{N} C_i e^{-\alpha_i t},\ N = 1, 2, 3 \tag{2}$$

with the constraint $P(0) = 1$ satisfied by $\sum_{i=1}^{N} C_i = 1$ (N = 1, 2, 3).

Goodness of fit for each simulation was determined by requiring that the coefficient of determination $R^2 > 0.95$. The fit with the smallest N satisfying this condition was chosen for further analysis. Single or double exponential fits were sufficient for most of the simulation results, with very few requiring a triple exponential fit. The characteristic IET time (τ_{IET} or $\langle t \rangle$) was calculated as the expectation value of the survival probability according to

$$\tau_{IET} = \langle t \rangle = \frac{\int_0^\infty tP(t)\,dt}{\int_0^\infty P(t)\,dt} \tag{3}$$

where $\int_0^\infty P(t)\,dt$ is the normalization constant.

Electron densities on the carboxylic acid linker group were determined from Mulliken population analyses[52] for each state to understand their correlation with the τ_{IET}.

3. RESULTS AND DISCUSSION

3.1. Ground State Structure and Spin Multiplicity. Complex **1** and its cyclometalated analogues **2**−**7** were optimized in both singlet and quintet spin states. $[Fe(tpy)_2]^{2+}$ (**1**) has been reported to be singlet[53−61] in the ground state. Comparison of the optimized structure of complex **1** with all of the crystal structures reported in the literature reveals that the B3LYP functional overestimates the bond lengths by 1.99−3.14% and underestimates the bite angles (N1−Fe−N3, N4−Fe−N6) by at most 0.60% (for details, see Table S2 and Figure S11 of the SI). Relatively small deviations between the calculated and experimental structures suggest that the chosen methodology is well suited for determination of molecular structures of Fe(II)-terpyridine-based complexes.

The B3LYP functional, however, incorrectly predicts quintet ground state multiplicity for complex **1**. The calculated $\Delta E_{HS/LS}$ is −1.24 kcal/mol suggesting a quintet ground state, whereas complex **1** is experimentally known to be singlet in its ground state.[53] This is not unusual for DFT calculations, because the relative stabilities of high-spin and low-spin states depend strongly on the amount of exact exchange in the DFT functional.[33,34] It was shown previously that the error in $\Delta E_{HS/LS}$ is similar for a set of structurally related complexes.[33] Structurally related complexes are defined as those that undergo similar changes in Fe-ligand bond lengths (ΔR) between the high-spin and low-spin structures. Complexes **1**−**7** are structurally related as they all have a similar ΔR (Table 1). Therefore, one can predict the ground state multiplicity of complexes **2**−**7** by comparing the calculated $\Delta E_{HS/LS}$ for these complexes to the $\Delta E_{HS/LS}$ obtained for complex **1**.

Data for $\Delta E_{HS/LS}$ relative to the admixture of exact exchange (c_1) in the B3LYP functional for complexes **1**−**7** were fit to a linear equation with the common slope of −171.87 kcal/mol (also see Figure S12, SI). The intercept for each complex, the coefficient of determination for each fit (R^2), and $\Delta\Delta E_{HS/LS}$, defined as

$$\Delta\Delta E_{HS/LS} = \Delta E_{HS/LS} - \Delta E^{\mathbf{1}}_{HS/LS} \tag{4}$$

where $\Delta E^{\mathbf{1}}_{HS/LS}$ is the $\Delta E_{HS/LS}$ for complex **1**, are given in Table 1. Because complex **1** is experimentally known to be singlet in its ground state, a positive $\Delta\Delta E_{HS/LS}$ value indicates an increase in the singlet−quintet energy gap and further stabilization of the singlet ground state in comparison to the singlet−quintet energy gap of complex **1**. As can be seen from Table 1,

DOI: 10.1021/ic502438g
Inorg. Chem. 2015, 54, 560−569

Table 1. Changes in the Fe-Ligand Bond Lengths (ΔR) between the High-Spin and Low-Spin Structures for Complexes 1−7, Along with Their Intercept, Coefficient of Determination (R^2), and $\Delta\Delta E_{HS/LS}$[a]

complex	ΔR (Å)	intercept (kcal/mol)	R^2	$\Delta\Delta E_{HS/LS}$ (kcal/mol)
1	0.22	32.25	0.98	0.0
2	0.23	40.21	1.00	8.0
3	0.25	41.45	1.00	9.2
4	0.27	40.65	1.00	8.4
5	0.28	49.85	1.00	17.6
6	0.29	45.29	0.99	13.0
7	0.26	51.55	0.99	19.3

[a]Common slope = −171.87 kcal/mol.

cyclometalation stabilizes the singlet state relative to the quintet state, and complexes **2**−**7** are all predicted to be singlet in their ground states. The extent of stabilization ranges from 8 to 19 kcal/mol and depends on the location and number of cyclometalation sites.

3.2. Ground State Electronic Structure. *3.2.1. Electronic Structure of Complexes 1−7.* The Kohn−Sham (KS) orbital energy levels for complexes **1**−**7** are shown in Figure 2. Solvent

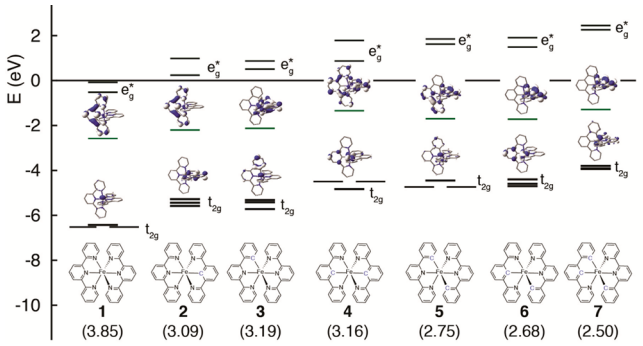

Figure 2. KS orbital energy levels of optimized complexes **1**−**7** after single-point energy calculations using the PCM model for water as the solvent. The optimized structures were obtained in vacuum using the B3LYP functional with ECP (SDD) on Fe and the 6-31G* basis set on C, H, and N. Numbers in parentheses are the HOMO−LUMO energy gap in eV. Metal-based orbitals are in black, and LUMO is in green. The t_{2g} orbital set is HOMO−HOMO−2. Note, there are several π^* ligand-centered orbitals between LUMO and e_g^* not pictured here.

effects (water) were accounted for in these calculations via the PCM model. An analogous energy level diagram obtained without the inclusion of solvent effects (vacuum) can be found in Figure S13 of the SI. The overall trend in HOMO−LUMO gaps is similar for calculations in water and in vacuum.

As can be seen in Figure 2, cyclometalation of complexes **2**−**7** destabilizes both HOMO and LUMO relative to those of complex **1**. The energies of HOMOs in complexes **2** and **3**, which have one metal−aryl bond, are destabilized by 1.15 and 1.11 eV, respectively. On the other hand, LUMOs of complexes **2** and **3** are destabilized by only 0.38 and 0.45 eV, respectively. Clearly, the extent of destabilization is greater for HOMO than LUMO in the cyclometalated complexes, leading to an overall decrease in the HOMO−LUMO gap. The HOMO−LUMO gap progressively decreases from 3.85 eV in complex **1** to 2.50 eV in complex **7** with three metal−aryl bonds. This correlates well with the observed trends in analogous cyclometalated Ru complexes, in which negative shifts of 0.5−0.8 eV were observed in the oxidation potentials, but reduction potentials decreased by only 0.2−0.4 eV.[62]

The three highest occupied KS orbitals, HOMO−2−HOMO, correspond to the t_{2g} orbital set for all of the complexes investigated. Aryl acts as a stronger π donor than pyridine with respect to the t_{2g} orbitals (compare t_{2g} orbitals of complexes **2** and **1** in Figure 3). Thus, the degeneracy of the t_{2g} orbital set is reduced in singly and doubly cyclometalated complexes, as can be seen in Figure 2.

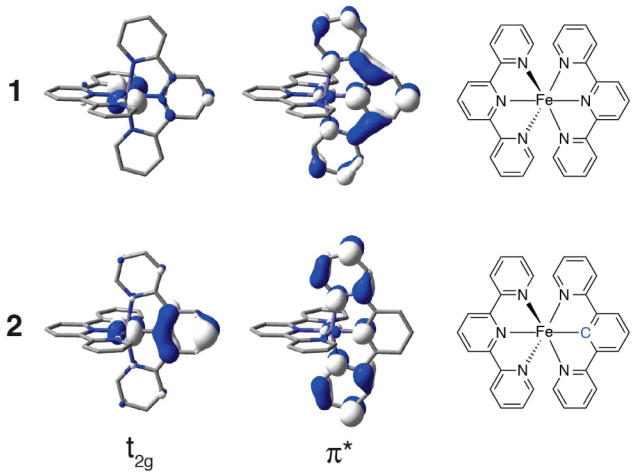

Figure 3. Selected t_{2g} and π^* orbitals of complexes **1** and **2**.

The four lowest unoccupied KS orbitals can be described as ligand-based π^* orbitals. Replacement of the pyridine by an aryl group in complexes **2**, **3**, and **5**−**7** significantly perturbs the nodal structure of LUMO−LUMO+3 relative to **1**, and they become predominantly localized on the pyridine rings (Figure 3). In the case of homoleptic complex **4**, the energy ordering of the two degenerate orbital pairs (LUMO,LUMO+1; LUMO+2,LUMO+3) is switched compared to that of complex **1**. Moreover, LUMO+2 and LUMO+3 have virtually no electron density on the central aryl ring. A detailed table of HOMO−2−LUMO+3 KS orbitals for **1**−**7** is provided in Figure S14 of the SI.

3.2.2. Electronic Structure of Complexes 1 and 4 Functionalized with Carboxylic Acid. The effects of functionalization with one (**1a**, **4a**), two (**1b**, **4b**), or three (**1c**, **4c**) carboxylic acid linkers on the energy levels of LUMO−LUMO+3 orbitals of complexes **1** and **4** are shown in Figure 4. The unoccupied orbitals of **1** and **4** stabilize when functionalized with the linkers. Interestingly, the extent of the orbital energy stabilization in complex **4** is more significant than in complex **1**. The energy ordering of the degenerate orbital pairs (LUMO+2,LUMO+3; LUMO,LUMO+1) is switched in complexes **4b** and **4c** compared to that in complexes **4** and **4a**. Nodal structures of all orbitals are available in Figure S15 of the SI.

The average percent electron density on carboxylic acid linkers in complexes **1a**−**c** and **4a**−**c** for LUMO and LUMO+2 orbitals is summarized in Table 2. The electron density was averaged over all carboxylic acid linkers attached to the central rings (4′ position) and side rings (4 and 4″ positions). Interestingly, there is virtually no electron density on carboxylic acid linkers attached to the aryl rings at the 4′ position in LUMO and LUMO+2. At the same time, the density on the linkers attached to the neighboring pyridyl rings (4 and 4″

DOI: 10.1021/ic502438g
Inorg. Chem. 2015, 54, 560−569

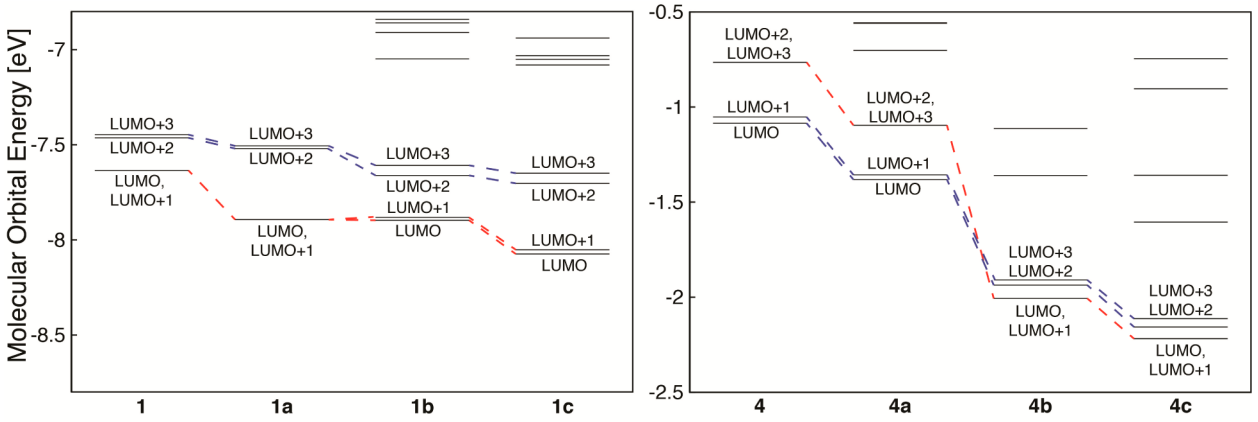

Figure 4. KS orbital energy levels for complexes **1** and **1a−c** (left) and **4** and **4a−c** (right). The complexes were fully optimized in vacuum using the B3LYP functional with SDD for Fe and the 6-31G* basis set for C, H, O, and N. The spin multiplicity is singlet. KS orbitals with the same nodal structure are connected by a dashed line.

Table 2. Average Percent of Electron Density on the Carboxylic Acid Linker Attached to the 4 and 4″ Positions on the Side Ring (Pyridyl) or 4′ Position on the Center Ring (1a−c = Pyridyl, 4a−c = Aryl)

	LUMO		LUMO+2	
complex	4′ position	4 and 4″ positions	4′ position	4 and 4″ positions
1a	3.2		0.1	
1b		1.3		1.2
1c	2.3	0.8	0.1	1.2
4a	0.0		1.1	
4b		5.8		4.9
4c	0.0	5.4	0.0	4.6

positions) increases relative to that of the parent complex. For example, the electron density on the linker attached to the side pyridyl rings (4 and 4″ positions) in complex **4b** increases from 1.3 to 5.8% (LUMO) and from 1.2 to 4.9% (LUMO+2) compared to that of complex **1b**. Similarly, the electron density on the linker attached to the side pyridyl rings (4 and 4″ positions) in complex **4c** increases from 0.8 to 5.4% (LUMO) and from 1.2 to 4.6% (LUMO+2) compared to that of complex **1c**.

3.3. Dye-TiO_2 Assemblies. Dye-TiO_2 assemblies were constructed on the basis of linker-TiO_2 models (Figure 5). Carboxylic acid was attached to the surface of TiO_2 via monodentate and bidentate attachment modes shown to be the most stable in previous computational and experimental studies.[63−65] Isonicotinic acid served as a linker model for **1a**-TiO_2 assemblies (see Figure 5 and Figure S17 of the SI), whereas a benzoic acid model was used to construct the **4a**-, **4b**-, **4c**-, and **4c**′-TiO_2 assemblies (Figure S18, SI).

The density of states calculated at the extended Hückel level of theory for **1a**-TiO_2 and **4a−c**′-TiO_2 assemblies in a monodentate attachment mode is shown in Figure 6. The density of states for the bidentate attachment mode is virtually identical and is provided in Figure S19 of the SI.

Dyes in all dye-TiO_2 assemblies investigated introduce occupied energy levels into the semiconductor band gap as well as a number of virtual energy levels into the conduction band of TiO_2. Both HOMO and LUMO energy levels of cyclometalated complexes **4a−c**′ are destabilized with respect to the HOMO and LUMO of parent complex **1a**. Although the HOMOs of cyclometalated complexes **4a−c**′ have significantly higher energy compared to that of their parent complex **1a**, they still remain below the edge of the conduction band of TiO_2.

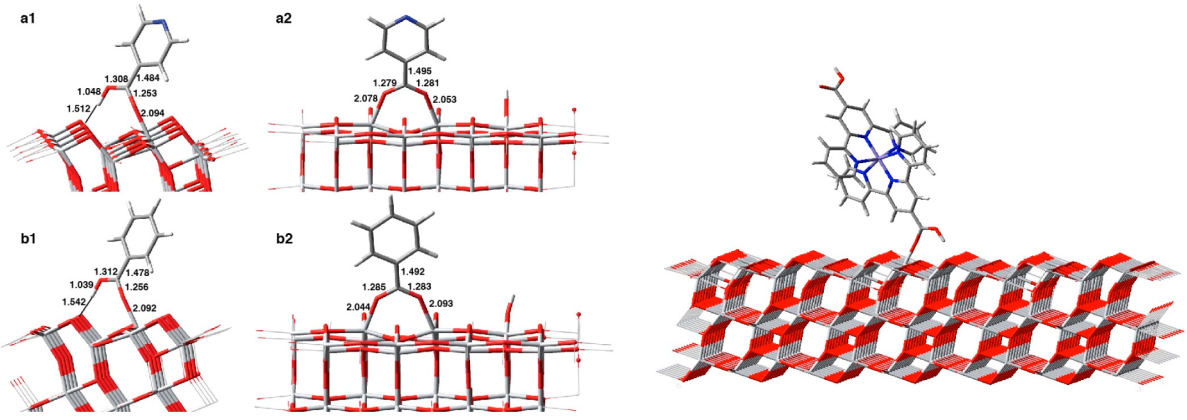

Figure 5. Linker models (left) consisting of a TiO_2 (101) surface with isonicotinic acid attached via a carboxylic acid linker in a monodentate (a1) and bidentate attachment mode (a2) (top row) and benzoic acid attached via a carboxylic acid linker in a monodentate (b1) and bidentate attachment mode (b2) (bottom row). An example of a dye-TiO_2 assembly of complex **1a** attached via monodentate carboxylic acid linkage is shown (right).

DOI: 10.1021/ic502438g
Inorg. Chem. 2015, 54, 560−569

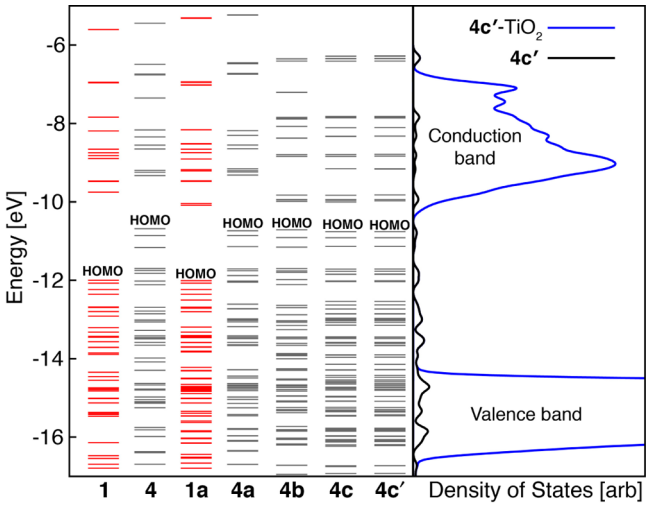

Figure 6. (left panel) EH orbital energy levels of **1** and **4** and their carboxylic acid functionalized analogues **1a**, **4a**, **4b**, **4c**, and **4c′**. (right panel) The blue line represents the total density of states for the whole-system (**4c′**-TiO_2) assemblies, and the black line represents the projected density of states for the dye only (**4c′**), convoluted using the Gaussian line shape with HWHM of 0.05 eV. The linker is attached to TiO_2 in a monodentate mode.

The nodal structures of the virtual EH MOs that were chosen to serve as initial states for the IET simulations are shown in Figure 7. The percent electron density on the carboxylic acid linker for each of these initial states is summarized in Table 3. Note that the percent electron densities on the linkers attached at the 4′ position of the ligand are negligible in the LUMO and LUMO+1 degenerate pair of complexes **4a** (0.0 and 0.2%, respectively) and **4c′** (0.0 and 0.7%, respectively). On the other hand, a significant amount of electron density is displayed on the linkers attached at the 4 and 4″ positions in the LUMO and LUMO+1 degenerate pairs of complexes **4b** (20.0 and 7.3%, respectively) and **4c** (23.6 and 4.1%, respectively). The nodal structure of virtual MOs and the percent electron density on the linker for dyes attached via a bidentate attachment mode are very similar to that of the monodentate case and can be found in Figure S20 and Table S12 of the SI.

Table 3. Percent of Electron Density on the Carboxylic Acid Linker Attached in a Monodentate Attachment Mode to the TiO_2 in the Functionalized Dyes 1a, 4a, 4b, 4c, and 4c′

	electron density on linker (%)				
complex	**1a**	**4a**	**4b**	**4c**	**4c′**
LUMO	22.3	0.0	20.0	23.6	0.0
LUMO+1	0.0	0.2	7.3	4.1	0.7
LUMO+2	0.0	0.1	0.0	0.0	0.0
LUMO+3	0.0	5.2	4.4	4.3	0.0
LUMO+4	19.8	48.0	1.9	0.0	54.6
LUMO+5	0.0	2.5	1.7	0.0	0.0
LUMO+6	0.0	0.0	1.4	2.0	0.0
LUMO+7	0.0	0.0	0.0	1.5	0.0

3.4. Interfacial Electron Transfer Simulations. Characteristic IET times (τ_{IET}) for the monodentate attachment modes for the dye-TiO_2 assemblies of complexes **1a**, **4a**, **4b**, **4c**, and **4c′** are summarized in Figure 8. The EH MOs are arranged in ascending order of their IET times for each dye-TiO_2 assembly. The black dashed line at 100 fs represents the characteristic time for the ISC process determined on the basis of previous experimental studies on Fe(II)-polypyridyl-based sensitizers.[14−16] Note that the ISC process in cyclometalated complexes **4a**, **4b**, **4c**, and **4c′** is expected to be slower than that of parent complex **1a** due to a positive $\Delta\Delta E_{HS/LS}$ as described in section 3.1. The actual ISC rate, however, is unknown.

Somewhat surprisingly, cyclometalation slows electron injection from the LUMO of complex **4a** by two orders of magnitude compared to that of complex **1a**, even though the LUMO of complex **4a** is aligned better with the CB of TiO_2

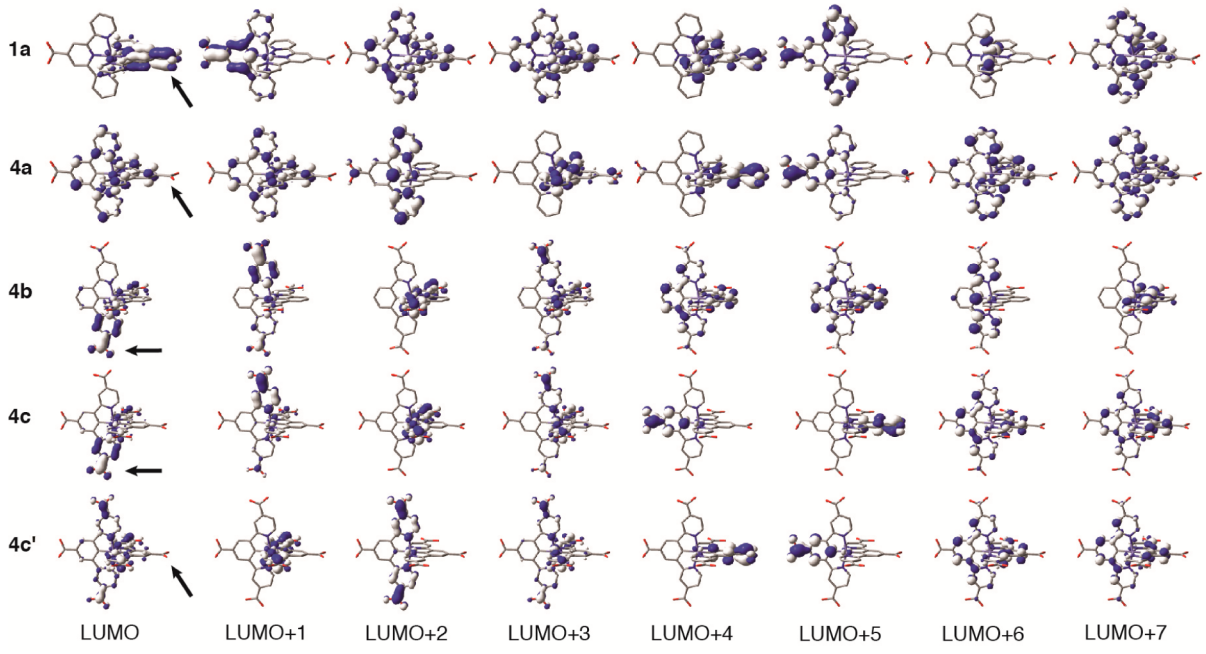

Figure 7. Nodal structures of LUMO−LUMO+7 EH orbitals employed as initial states for IET simulations in **1a**-TiO_2 and **4a**−**c′**-TiO_2 assemblies with a monodentate binding mode. The linker used to attach the dye to TiO_2 is shown using an arrow.

DOI: 10.1021/ic502438g
Inorg. Chem. 2015, 54, 560−569

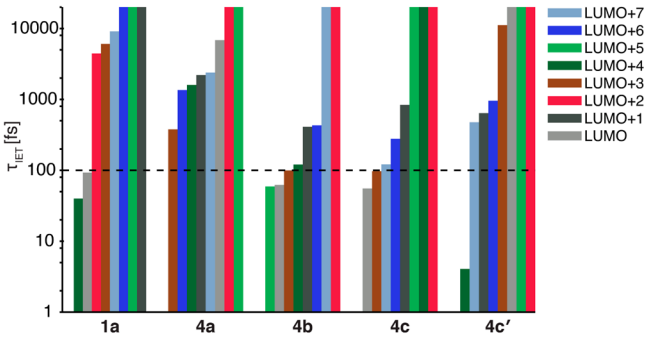

Figure 8. Characteristic IET times (τ_{IET}) for LUMO−LUMO+7 Hückel orbitals of dye-TiO_2 assemblies of **1a**, **4a**, **4b**, **4c**, and **4c**′ (monodentate attachment mode) obtained from exponential fits to the survival probability. The dashed line at 100 fs represents the characteristic ISC time for complex **1a**. ISC rates for complexes **4a**−**c**′ are not known.

than the LUMO of complex **1a** (Figure 6). The survival probability plots and nodal structures for LUMOs of complexes **1a** and **4a** shown in Figure 9 indicate that the slow rate of IET

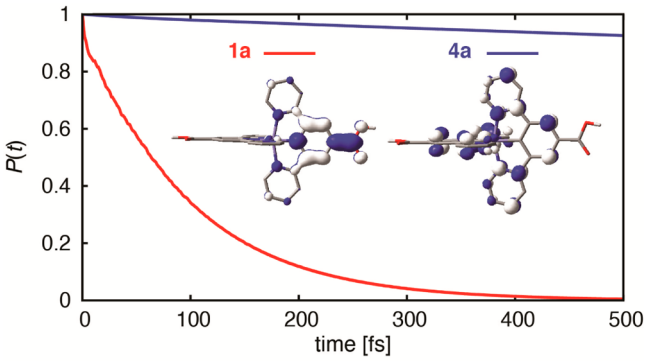

Figure 9. Survival probability of LUMOs of parent complex **1a** and its cyclometalated analogue **4a**.

for complex **4a** is due to the lack of electron density on the carboxylic acid linker attached to the aryl ring. Moreover, the fastest characteristic IET time obtained for cyclometalated complex **4a** (377 fs, LUMO+3 initial state) is 1 order of magnitude larger than the fastest characteristic IET time obtained for complex **1a** (39 fs, LUMO+4 initial state). Overall, cyclometalation negatively impacts the IET in **4a**-TiO_2 assemblies.

In contrast to complex **1a**, complexes **4b** and **4c** display a significant amount of electron density on the carboxylic acid linkers that anchor these dyes to the TiO_2 surface (Table 3). The calculated IET rates in **4b**-TiO_2 and **4c**-TiO_2 assemblies originating in the dye's LUMO improve significantly compared to that of **4a**-TiO_2. More importantly, several initial states in each of these assemblies achieve subpicosecond IET rates.

The IET in the **4c**′-TiO_2 assembly is not as optimal as in the **4b**-TiO_2 and **4c**-TiO_2 assemblies but is more efficient than that of the **4a**-TiO_2 assembly. Note that whereas **4c**′-TiO_2 and **4c**-TiO_2 model the attachment of the same dye to the semiconductor surface, the dye in the **4c**′-TiO_2 assembly is attached to the surface via the carboxylic acid at the 4′ position rather than at the 4 position. The drop in IET efficiency is most likely due to the decrease in electron density on the linker at the 4′ position.

Characteristic IET times were also calculated for dye-TiO_2 assemblies with the carboxylic acid linker in the bidentate attachment mode. Interestingly, the IET in such systems is less efficient than in assemblies with the monodentate binding mode. The overall trends in the behavior, however, are the same for both attachment modes. These include deterioration of IET in the **4a**-TiO_2 assembly and the increase in IET efficiency in the **4b**-TiO_2 and **4c**-TiO_2 assemblies relative to that of the **1a**-TiO_2 system. All data related to dye-TiO_2 assemblies with the bidentate attachment mode can be found in Table S24 and Figure S21 of the SI.

In summary, IET is clearly facilitated by an increase in the electron density on the carboxylic acid linker, and the position of the linker group (4 and 4″ vs 4′) is an important factor in determining the efficiency of IET in the cyclometalated dye-semiconductor assemblies.

3.5. Consequences of Cyclometalation for Dye Sensitization. An ideal photosensitizer for DSSCs will be chemically stable, absorb light over a wide range of visible wavelengths, and undergo efficient IET into the semiconductor.[1] Until now, the main obstacle to the utilization of Fe(II)-polypyridines as photosensitizers in DSSCs has been the very short excited state lifetime of their photoactive metal-to-ligand charge transfer states due to the ultrafast ISC into the manifold of low-lying ligand-field states.[14,15]

Our initial calculations on $[Fe(tpy)_2]^{2+}$ and related complexes suggest that cyclometalation may have several beneficial consequences. First, the presence of Fe−C bonds will stabilize the singlet ground state and increase the $^1A-^5T$ energy gap in these complexes, which could have a positive impact on the lifetime of the MLCT states. Recently, Wärnmark and co-workers observed an unusually long-lived MLCT excited state in an Fe(II) complex with four Fe−C bonds, utilizing N-heterocyclic carbenes as ligands.[20,21] This was later explained as a consequence of an increase in the $^1A-^5T$ gap in these complexes.[20] It is worth noting that the magnitude of the increase in the $^1A-^5T$ gap in the complexes studied here depends on both the number of Fe−C bonds and the site of cyclometalation. For example, the $^1A-^5T$ gap increases by approximately 8−9 kcal/mol for complexes **2** and **3** with a single Fe−C bond relative to complex **1**. The $^1A-^5T$ gap in doubly cyclometalated complexes increases by either 8 kcal/mol in complex **4**, in which the two Fe−C bonds are on the same axis, or 13−18 kcal/mol when the two cyclometalated sites lie along different axes, such as in complexes **5** and **6**. The increase in the $^1A-^5T$ gap in triply cyclometalated complex **7** is only marginally higher than in complex **5**. Overall, cyclometalation of the side rings of the terpyridine ligand seems to have a much bigger impact on the $^1A-^5T$ energy gap than cyclometalation of the central ring (compare $\Delta\Delta E_{HS/LS}$ for complexes **4**, **5**, and **6** in Table 1).

Additional consequences of cyclometalation for ground state electronic structure include reduced degeneracy of the t_{2g} orbital set, a decrease of the HOMO−LUMO gap, and destabilization of both HOMO and LUMO energies. Because the MLCT transitions that constitute a large portion of the visible spectrum in these complexes originate in the metal-centered t_{2g} orbitals, the reduced degeneracy will likely result in broadening of the absorption spectrum. A decrease in the HOMO−LUMO gap might also result in a red-shift of their absorption spectra in comparison to that of complex **1**. Both of these changes should be beneficial for light harvesting, as they would result in absorption over a wider range of the visible

DOI: 10.1021/ic502438g
Inorg. Chem. 2015, 54, 560−569

spectrum. Destabilization of both HOMO and LUMO energies could also be beneficial for light harvesting, as it would place the LUMO higher into the conduction band of TiO_2, thus increasing the driving force for IET.

On the other hand, destabilization of HOMO and LUMO energies resulting in a large change in the redox potentials of cyclometalated dyes could cause significant problems for IET. For dye sensitization to work properly, the dye needs to insert its occupied energy levels (including the HOMO) into the band gap of TiO_2, whereas the lowest energy virtual orbitals have to be aligned with the conduction band of TiO_2. Significant changes in the redox potential of the dyes caused by cyclometalation could cause the HOMO and LUMO to be misaligned with the valence and conduction bands of TiO_2. Our semiempirical calculations suggest that doubly cyclometalated dyes will be able to sensitize TiO_2 despite the shift in the HOMO and LUMO energy levels (Figure 8). It is unclear, however, whether the energy levels of triply cyclometalated dyes will still be properly aligned with the TiO_2 energy bands.

Another concern related to cyclometalation is the positioning of the ground state oxidation potential of the dye compared to the redox coupling of the I^-/I_3^-electrolyte (~0.5 eV relative to the normal hydrogen electrode). The regeneration of dye in DSSCs with the I^-/I_3^- electrolyte may become difficult or impossible because the energy of HOMO becomes destabilized (Figure 2),[62] and the use of alternative redox shuttles might be necessary to regenerate cyclometalated Fe(II)-polypyridines.[66] Accurate calculations of redox potentials of these new cyclometalated dyes are needed to further investigate this issue.

Finally, it is important to consider IET efficiency in cyclometalated dye-TiO_2 assemblies. Previous experimental and computational studies suggested that both the amount of electron density on the linker as well as the placement of virtual orbitals involved in photoexcitation with respect to the edge of the conduction band of the semiconductor influence the rate of IET in dye-semiconductor assemblies.[2,9,17,18,67,68] In general, electron density on the linker facilitates electronic coupling between an excited state of the dye and the acceptor states in the conduction band semiconductor and results in faster IET rates.[2,19] The placement of the virtual energy levels high in the CB of the semiconductor improves the driving force for IET.[19] For the cyclometalated complexes investigated here, there is a trade-off between the percent of electron density on the linker group and the energy of virtual orbitals. In complex **4a** for example, the LUMO−LUMO+1 pair has high energy that places it well into the CB of TiO_2 but has significantly reduced electron density. The energy of LUMO in complexes **4b** and **4c** is lower compared to that of complex **4a**, whereas the electron density increases in the former relative to that of the latter. Both the energy of LUMO and the electron density on the carboxylic acid linkers at the 4′ position are reduced in complex **4c**′.

In summary, our results suggest that the cyclometalated complexes will display an ability to sensitize TiO_2 at least equal to that of parent complex **1** assuming that the carboxylic acid linker is attached to a pyridine rather than an aryl ring.

4. CONCLUSIONS

Cyclometalated Fe(II) complexes based on $[Fe(tpy)_2]^{2+}$, in which one, two, or three neutral pyridine ligands were substituted by negative aryl ligands, were investigated as possible photosensitizers in DSSCs. The aim of this work was to determine whether cyclometalation stabilizes the singlet ground state and if the cyclometalated complexes can sensitize TiO_2.

Density functional theory calculations performed on complexes **1**−**7** suggest that cyclometalation stabilizes the ^{1}A ground state and increases the energy difference between the ^{1}A and ^{5}T states by 8−19 kcal/mol. The amount of ^{1}A stabilization depends on the total number (one, two, or three) and position (center or side) of the aryl groups. Cyclometalation therefore has the potential to decrease the ISC rate between ^{1,3}MLCT and ^{5}MC states, thus increasing the lifetime of photoactive MLCT states. Further computational studies investigating relative energetic ordering and potential energy surfaces of all electronic states involved in the intersystem crossing cascade (^{1}A, ^{1}MLCT, ^{3}MLCT, ^{3}T, ^{5}T) are necessary to obtain a better understanding of the ISC processes in these systems.

Cyclometalation also has consequences for the light-harvesting properties of Fe(II)-polypyridine complexes. Both HOMO and LUMO of complexes **2**−**7** are destabilized in comparison to that of complex **1**. The extent of destabilization is greater for HOMO than LUMO, leading to a decrease in the HOMO−LUMO gap. Cyclometalated complexes will therefore likely absorb light at lower energy wavelengths. The degeneracy of the t_{2g} orbital set is also reduced with cyclometalation, which could lead to absorption over a broader range of visible wavelengths.

The increase in the HOMO and LUMO energies of complexes **2**−**7** suggests that the redox potentials of cyclometalated dyes will differ from that of complex **1**. Fine-tuning of the ligand π^* and t_{2g} energy levels may therefore be necessary to ensure that the HOMO and LUMO of the cyclometalated dyes are properly aligned with the energy bands of the TiO_2 semiconductor and that the oxidized dyes can be reduced by the electrolyte used in the DSSC.

Quantum dynamics simulations of IET in **1**-TiO_2 and **4**-TiO_2 assemblies indicate that cyclometalated complexes will sensitize the TiO_2 semiconductor upon photoexcitation with an efficiency similar to or better than that of the $[Fe(tpy)_2]^{2+}$ parent complex. The carboxylic acid linker should be attached to the pyridine group rather than the aryl group of the ligand to facilitate efficient IET.

In conclusion, cyclometalation can potentially improve absorption properties of Fe(II) dyes and may slow the ISC rate by destabilizing the ^{5}T state relative to the ^{1}A ground state. Cyclometalated Fe(II) complexes will display an ability to sensitize TiO_2 at least equal to that of parent complex **1**, but only when the semiconductor anchoring group is attached to a pyridine rather than an aryl ring. Although cyclometalation appears to be a promising way to improve the sensitization capabilities of Fe(II)-polypyridines, further theoretical and experimental work is needed to confirm these observations.

■ ASSOCIATED CONTENT

Ⓢ Supporting Information

The coordination environment (bond lengths and angles) of Fe in singlet- and quintet-optimized structures and coordinates of complexes **1**−**7**; KS orbital energy levels of complexes **1**−**7** optimized in vacuum; spin contaminations of quintet-optimized structures of complexes **1**−**7**; $\Delta E_{HS/LS}$ relative to exact exchange admixtures for **1**−**7**; EH MOs of complex **4a** using reparameterized invariance principles (IPs) compared to DFT MOs and EH MOs using default IPs; dye-TiO_2 assemblies of complexes **1a**, **4a**, **4b**, **4c**, and **4c**′ with linkers attached to TiO_2

DOI: 10.1021/ic502438g
Inorg. Chem. 2015, 54, 560−569

in bidentate and monodentate binding modes; density states of complexes **1**, **4**, **1a**, **4a**, **4b**, **4c**, and **4c′** in the bidentate binding mode; EH MOs and electron density on the linker involved in the bidentate mode of binding for complexes **1**, **4**, **1a**, **4a**, **4b**, **4c**, and **4c′**; and IET results of dye-TiO_2 assemblies of **1a**, **4a**, **4b**, **4c**, and **4c′** in monodentate and bidentate binding modes. This material is available free of charge via the Internet at http://pubs.acs.org.

AUTHOR INFORMATION

Corresponding Author

*E-mail: ejakubi@ncsu.edu.

Notes

The authors declare no competing financial interest.

ACKNOWLEDGMENTS

This research was supported by Army Research Office Grant 59842-CH-II and North Carolina State University. This work was performed in part at the Center for Integrated Nanotechnologies, which is a user facility operated for the U.S. Department of Energy Office of Science by the Los Alamos National Laboratory (Contract DE-AC52-06NA25396) and the Sandia National Laboratories (Contract DE-AC04-94AL85000). D.N.B. also acknowledges support from the U.S. Department of Education Graduate Assistantship in Areas of National Need (GAANN) fellowship program at North Carolina State University. We gratefully acknowledge Prof. Victor S. Batista (Yale University) for providing a copy of the code for IET simulations. We also thank Dr. Reginaldo C. Rocha (Los Alamos National Laboratory) for helpful discussions.

REFERENCES

(1) Ardo, S.; Meyer, G. J. *Chem. Soc. Rev.* **2009**, *38*, 115.
(2) Clifford, J. N.; Martinez-Ferrero, E.; Viterisi, A.; Palomares, E. *Chem. Soc. Rev.* **2011**, *40*, 1635.
(3) Goetzberger, A.; Hebling, C.; Schock, H. W. *Mater. Sci. Eng., R* **2003**, *40*, 1.
(4) Nazeeruddin, M. K.; Kay, A.; Rodicio, I.; Humphry-Baker, R.; Mueller, E.; Liska, P.; Vlachopoulos, N.; Grätzel, M. *J. Am. Chem. Soc.* **1993**, *115*, 6382.
(5) O'Regan, B.; Grätzel, M. *Nature* **1991**, *353*, 737.
(6) Kalyanasundaram, K.; Grätzel, M. *Coord. Chem. Rev.* **1998**, *177*, 347.
(7) Grätzel, M. *Inorg. Chem.* **2005**, *44*, 6841.
(8) Chen, C.-Y.; Wang, M.; Li, J.-Y.; Pootrakulchote, N.; Alibabaei, L.; Ngoc-le, C.-H.; Decoppet, J.-D.; Tsai, J.-H.; Grätzel, C.; Wu, C.-G.; Zakeeruddin, S. M.; Grätzel, M. *ACS Nano* **2009**, *3*, 3103.
(9) Ferrere, S.; Gregg, B. A. *J. Am. Chem. Soc.* **1998**, *120*, 843.
(10) Ferrere, S. *Inorg. Chim. Acta* **2002**, *329*, 79.
(11) Yang, M.; Thompson, D. W.; Meyer, G. J. *Inorg. Chem.* **2000**, *39*, 3738.
(12) Ghosh, H. N.; Asbury, J. B.; Weng, Y.; Lian, T. *J. Phys. Chem. B* **1998**, *102*, 10208.
(13) Creutz, C.; Chou, M.; Netzel, T. L.; Okumura, M.; Sutin, N. *J. Am. Chem. Soc.* **1980**, *102*, 1309.
(14) Monat, J. E.; McCusker, J. K. *J. Am. Chem. Soc.* **2000**, *122*, 4092.
(15) Juban, E. A.; Smeigh, A. L.; Monat, J. E.; McCusker, J. K. *Coord. Chem. Rev.* **2006**, *250*, 1783.
(16) Smeigh, A. L.; Creelman, M.; Mathies, R. A.; McCusker, J. K. *J. Am. Chem. Soc.* **2008**, *130*, 14105.
(17) Bowman, D. N.; Blew, J. H.; Tsuchiya, T.; Jakubikova, E. *Inorg. Chem.* **2013**, *52*, 14449.
(18) Bowman, D. N.; Blew, J. H.; Tsuchiya, T.; Jakubikova, E. *Inorg. Chem.* **2013**, *52*, 8621.
(19) Bowman, D. N.; Mukherjee, S.; Barnes, L. J.; Jakubikova, E. *J. Phys.: Condens. Matter* **2014**, accepted for publication.
(20) Fredin, L. A.; Pápai, M.; Rozsályi, E.; Vankó, G.; Wärnmark, K.; Sundström, V.; Persson, P. *J. Phys. Chem. Lett.* **2014**, *5*, 2066.
(21) Liu, Y.; Harlang, T.; Canton, S. E.; Chabera, P.; Suarez-Alcantara, K.; Fleckhaus, A.; Vithanage, D. A.; Goransson, E.; Corani, A.; Lomoth, R.; Sundstrom, V.; Warnmark, K. *Chem. Commun. (Cambridge, U.K.)* **2013**, *49*, 6412.
(22) Jamula, L. L.; Brown, A. M.; Guo, D.; McCusker, J. K. *Inorg. Chem.* **2014**, *53*, 15.
(23) Dixon, I. M.; Khan, S.; Alary, F.; Boggio-Pasqua, M.; Heully, J.-L. *Dalton Trans.* **2014**, *43*, 15898.
(24) Dixon, I. M.; Alary, F.; Boggio-Pasqua, M.; Heully, J.-L. *Inorg. Chem.* **2013**, *52*, 13369.
(25) Becke, A. D. *J. Chem. Phys.* **1993**, *98*, 1372.
(26) Becke, A. D. *J. Chem. Phys.* **1993**, *98*, 5648.
(27) Lee, C.; Yang, W.; Parr, R. G. *Phys. Rev. B* **1988**, *37*, 785.
(28) Kaupp, M.; Schleyer, P. v. R.; Stoll, H.; Preuss, H. *J. Chem. Phys.* **1991**, *94*, 1360.
(29) Hariharan, P. C.; Pople, J. A. *Theor. Chim. Acta* **1973**, *28*, 213.
(30) Hehre, W. J.; Ditchfield, R.; Pople, J. A. *J. Chem. Phys.* **1972**, *56*, 2257.
(31) Davidson, E. R. *Rev. Mod. Phys.* **1972**, *44*, 451.
(32) Frisch, M. J.; Trucks, G. W.; Schlegel, H. B.; Scuseria, G. E.; Robb, M. A.; Cheeseman, J. R.; Scalmani, G.; Barone, V.; Mennucci, B.; Petersson, G. A.; Nakatsuji, H.; Caricato, M.; Li, X.; Hratchian, H. P.; Izmaylov, A. F.; Bloino, J.; Zheng, G.; Sonnenberg, J. L.; Hada, M.; Ehara, M.; Toyota, K.; Fukuda, R.; Hasegawa, J.; Ishida, M.; Nakajima, T.; Honda, Y.; Kitao, O.; Nakai, H.; Vreven, T.; Montgomery, J. A., Jr.; Peralta, J. E.; Ogliaro, F.; Bearpark, M.; Heyd, J. J.; Brothers, E.; Kudin, K. N.; Staroverov, V. N.; Kobayashi, R.; Normand, J.; Raghavachari, K.; Rendell, A.; Burant, J. C.; Iyengar, S. S.; Tomasi, J.; Cossi, M.; Rega, N.; Millam, M. J.; Klene, M.; Knox, J. E.; Cross, J. B.; Bakken, V.; Adamo, C.; Jaramillo, J.; Gomperts, R.; Stratmann, R. E.; Yazyev, O.; Austin, A. J.; Cammi, R.; Pomelli, C.; Ochterski, J. W.; Martin, R. L.; Morokuma, K.; Zakrzewski, V. G.; Voth, G. A.; Salvador, P.; Dannenberg, J. J.; Dapprich, S.; Daniels, A. D.; Farkas, Ö.; Foresman, J. B.; Ortiz, J. V.; Cioslowski, J.; Fox, D. J. *Gaussian 09*, revision D.01; Gaussian, Inc.: Wallingford, CT, 2009.
(33) Bowman, D. N.; Jakubikova, E. *Inorg. Chem.* **2012**, *51*, 6011.
(34) Reiher, M. *Inorg. Chem.* **2002**, *41*, 6928.
(35) Kresse, G.; Furthmüller, J. *Phys. Rev. B* **1996**, *54*, 11169.
(36) Kresse, G.; Furthmüller, J. *Comput. Mater. Sci.* **1996**, *6*, 15.
(37) Kresse, G.; Hafner, J. *Phys. Rev. B* **1993**, *47*, 558.
(38) Kresse, G.; Hafner, J. *Phys. Rev. B* **1994**, *49*, 14251.
(39) Perdew, J. P.; Burke, K.; Ernzerhof, M. *Phys. Rev. Lett.* **1996**, *77*, 3865.
(40) Perdew, J. P.; Burke, K.; Ernzerhof, M. *Phys. Rev. Lett.* **1997**, *78*, 1396.
(41) Blöchl, P. E. *Phys. Rev. B* **1994**, *50*, 17953.
(42) Kabsch, W. *Acta Crystallogr., Sect. A* **1978**, *34*, 827.
(43) Jakubikova, E.; Snoeberger, R. C., III; Batista, V. S.; Martin, R. L.; Batista, E. R. *J. Phys. Chem. A* **2009**, *113*, 12532.
(44) Jakubikova, E.; Martin, R. L.; Batista, E. R. *Inorg. Chem.* **2010**, *49*, 2975.
(45) Rego, L. G. C.; Batista, V. S. *J. Am. Chem. Soc.* **2003**, *125*, 7989.
(46) Abuabara, S. G.; Rego, L. G. C.; Batista, V. S. *J. Am. Chem. Soc.* **2005**, *127*, 18234.
(47) Wadman, S. H.; van der Geer, E. P. L.; Havenith, R. W. A.; Klein Gebbink, R. J. M.; van Klink, G. P. M.; van Koten, G. *J. Organomet. Chem.* **2008**, *693*, 3188.
(48) Zhou, X.; Ren, A.-M.; Feng, J.-K. *J. Organomet. Chem.* **2005**, *690*, 338.
(49) Braterman, P. S.; Song, J. I.; Peacock, R. D. *Inorg. Chem.* **1992**, *31*, 555.
(50) Jakubikova, E.; Chen, W.; Dattelbaum, D. M.; Rein, F. N.; Rocha, R. C.; Martin, R. L.; Batista, E. R. *Inorg. Chem.* **2009**, *48*, 10720.
(51) Alvarez, S. *Table of parameters for Extended Hückel Calculations*; Universitat de Barcelona: Barcelona, Spain, 1993.

DOI: 10.1021/ic502438g
Inorg. Chem. 2015, 54, 560−569

(52) Mulliken, R. S. *J. Chem. Phys.* **1955**, *23*, 1833.
(53) Chambers, J.; Eaves, B.; Parker, D.; Claxton, R.; Ray, P. S.; Slattery, S. J. *Inorg. Chim. Acta* **2006**, *359*, 2400.
(54) Baba, Y.; Yasuda, H.; Kawakita, K.; Ueyama, N. *Macromolecules* **2003**, *36*, 7953.
(55) Baker, A.; Goodwin, H. *Aust. J. Chem.* **1985**, *38*, 207.
(56) Danjo, H.; Hirata, K.; Noda, M.; Uchiyama, S.; Fukui, K.; Kawahata, M.; Azumaya, I.; Yamaguchi, K.; Miyazawa, T. *J. Am. Chem. Soc.* **2010**, *132*, 15556.
(57) Kabir, M. K.; Tobita, H.; Matsuo, H.; Nagayoshi, K.; Yamada, K.; Adachi, K.; Sugiyama, Y.; Kitagawa, S.; Kawata, S. *Cryst. Growth Des.* **2003**, *3*, 791.
(58) Laine, P.; Gourdon, A.; Launay, J. P. *Inorg. Chem.* **1995**, *34*, 5138.
(59) Oshio, H.; Spiering, H.; Ksenofontov, V.; Renz, F.; Gütlich, P. *Inorg. Chem.* **2001**, *40*, 1143.
(60) Ovens, J. S.; Geisheimer, A. R.; Bokov, A. A.; Ye, Z.-G.; Leznoff, D. B. *Inorg. Chem.* **2010**, *49*, 9609.
(61) Tershansy, M. A.; Goforth, A. M.; Peterson, L., Jr.; Burns, M. C.; Smith, M. D.; zur Loye, H.-C. *Solid State Sci.* **2007**, *9*, 895.
(62) Bomben, P. G.; Robson, K. C. D.; Sedach, P. A.; Berlinguette, C. P. *Inorg. Chem.* **2009**, *48*, 9631.
(63) Persson, P.; Lunell, S. *Sol. Energy Mater. Sol. Cells* **2000**, *63*, 139.
(64) Nilsing, M.; Persson, P.; Ojamäe, L. *Chem. Phys. Lett.* **2005**, *415*, 375.
(65) Labat, F.; Adamo, C. *J. Phys. Chem. C* **2007**, *111*, 15034.
(66) Hamann, T. W. *Dalton Trans.* **2012**, *41*, 3111.
(67) Hagfeldt, A.; Boschloo, G.; Sun, L.; Kloo, L.; Pettersson, H. *Chem. Rev.* **2010**, *110*, 6595.
(68) Asbury, J. B.; Anderson, N. A.; Hao, E.; Ai, X.; Lian, T. *J. Phys. Chem. B* **2003**, *107*, 7376.

DOI: 10.1021/ic502438g
Inorg. Chem. 2015, 54, 560−569